

Binary Formation with Different Metallicities: Dependence on Initial Conditions

Masahiro N. Machida^{1,2*}, Kazuyuki Omukai², Tomoaki Matsumoto³ and Shu-ichiro Inutsuka

¹*Department of Physics, Graduate School of Science, Kyoto University, Sakyo-ku, Kyoto 606-8502, Japan*

²*National Astronomical Observatory of Japan, Mitaka, Tokyo 181-8588, Japan*

³*Faculty of Humanity and Environment, Hosei University, Fujimi, Chiyoda-ku, Tokyo 102-8160, Japan*

22 June 2018

ABSTRACT

The fragmentation process in collapsing clouds with various metallicities is studied using three-dimensional nested-grid hydrodynamics. Initial clouds are specified by three parameters: cloud metallicity, initial rotation energy and initial cloud shape. For different combinations of these parameters, we calculate 480 models in total and study cloud evolution, fragmentation conditions, orbital separation and binary frequency. For the cloud to fragment during collapse, the initial angular momentum must be higher than a threshold value, which decreases with decreasing metallicity. Although the exact fragmentation conditions depend also on the initial cloud shape, this dependence is only modest. Our results indicate a higher binary frequency in lower-metallicity gas. In particular, with the same median rotation parameter as in the solar neighbourhood, a majority of stars are born as members of binary/multiple systems for $< 10^{-4} Z_{\odot}$. With initial mass $< 0.1 M_{\odot}$, if fragments are ejected in embryo from the host clouds by multi-body interaction, they evolve to substellar-mass objects. This provides a formation channel for low-mass stars in zero- or low-metallicity environments.

Key words: binaries: general—cosmology: theory — galaxies: formation — hydrodynamics—stars: formation

1 INTRODUCTION

Observations in the solar neighbourhood have shown a high binary frequency (Abt 1983; Duquennoy & Mayor 1991; Fischer & Marcy 1992; see also the review of Goodwin et al. 2007). Because the binary frequency in star-forming regions is even higher than that in the field (Mathieu 1994), a majority of stars is believed to be born as binaries. However, the observable star-forming regions are limited in the solar neighbourhood and thus at metallicity comparable to the solar abundance (i.e., $Z = Z_{\odot}$). We do not know the binary frequency in lower ($Z < Z_{\odot}$) or zero ($Z = 0$) metallicity environments.

Binary stars have important roles in many astrophysical contexts. They are considered to be related to a pollution of extremely metal-poor stars (Suda et al. 2004; Lucatello et al. 2005; Komiya et al. 2006), progenitors of gamma-ray bursts (Bromm & Loeb 2006) and Type Ia supernovae (Nomoto, Thielemann, & Yokoi 1984), the evolution of globular clus-

ters (Sugimoto & Bettwieser 1983; Makino 1996) and the source of gravitational waves (e.g., Seto 2002).

The formation process of binary (or multiple) systems in collapsing clouds with $Z = Z_{\odot}$ has been studied by means of three-dimensional hydrodynamics (see the reviews of Bodenheimer et al. 2000 and Goodwin et al. 2007). They showed that fragmentation occurs after the cloud becomes optically thick at $n > 10^{11} \text{ cm}^{-3}$, leading to formation of binary or multiple stellar systems. Whether fragmentation occurs depends sensitively on the initial condition, e.g. the initial angular velocity and cloud shapes (Goodwin et al. 2007). Thus, to determine the fragmentation condition and binary frequency, we need to calculate cloud evolution for a number of models.

On the other hand, star formation in primordial clouds has also been investigated by cosmological three-dimensional simulations (Abel et al. 2002; Bromm et al. 2002; Yoshida et al. 2006). Recently, Yoshida et al. (2008) succeeded in calculating cloud evolution up to protostar formation ($n \simeq 10^{21} \text{ cm}^{-3}$) and demonstrated that fragmentation does not occur. However, cosmological simulations tend to calculate only a single clump with the lowest angular momentum, which collapses first. This setting prevents the cloud from fragmenting, because binaries form in clouds

* E-mail: machidam@scphys.kyoto-u.ac.jp (MNM); omukai@th.nao.ac.jp (KO); matsui@i.hosei.ac.jp (TM); inutsuka@tap.scphys.kyoto-u.ac.jp(SI)

with a high angular momentum. Therefore, if we consider not only the clouds collapsing first but also those forming at a later time, binaries may form within them. In fact, Saigo et al. (2004) and Machida et al. (2008a) calculated the collapse of primordial clouds with different degrees of initial rotation, and showed the possibility of fragmentation and binary formation. Clark et al. (2008) demonstrated fragmentation of zero- and low-metallicity turbulent clouds by three-dimensional hydrodynamics and showed that the fragments acquire angular momentum from turbulence.

The cloud evolution and fragmentation condition only for primordial clouds were investigated in Machida et al. (2008a). Machida (2008b) investigated the evolution of clouds with various metallicities and showed that the binary frequency increases as the metallicity decreases. However, in this study, almost spherical clouds are adopted as the initial states. As Goodwin et al. (2007) pointed out, slight differences in the initial conditions may affect cloud evolution and its fragmentation process. In the present paper, we investigate cloud evolution with various metallicities for a wider range of initial conditions than Machida (2008b). Especially, to investigate the effect of the cloud shape on fragmentation, in some models, we adopt a strongly distorted structure as the initial state. In total, we have calculated 480 models with combinations of three parameters: the cloud metallicity (Z), initial rotation energy (β_0), and initial amplitude of the non-axisymmetric perturbation (A_ϕ) corresponding to the initial cloud shape. The large number of models makes it possible to discuss the fragmentation condition and epoch, separation between fragments for clouds with different metallicities.

This paper is organized as follows. The basics of our model are summarized in §2. The thermal evolution of clouds with different metallicities is shown in §3. Then, we describe the dependence on initial cloud parameters in §4. In §5, we discuss some uncertainties and possible fates of the fragments. Finally, we summarize our results in §6.

2 MODEL SETTINGS

We solve the equations of hydrodynamics adopting a nested grid method to ensure the Jeans condition of the collapsing cloud. Each level of a rectangular grid has the same number of cells of $128 \times 128 \times 8$ (for details, see Machida et al. 2005a; 2006a). The energy equation is not solved: instead, we adopt the barotropic relations for pressure as a function of density calculated with one-zone models by Omukai et al. (2005). Figure 1 shows these relations for different metallicities as a function of the number density.

As an initial condition, we take a spherical cloud with density 1.4 times higher than hydrostatic equilibrium with external pressure (i.e. the so-called critical Bonnor–Ebert sphere; see Bonnor 1956; Ebert 1955). The initial central density is taken as $n_{c,0} = 1.4 \times 10^4 \text{ cm}^{-3}$. The critical radius of the Bonnor–Ebert sphere is $R_c = 6.45 c_s / [4\pi G \rho_{BE}(0)]^{1/2}$. Outside this radius, a uniform gas density of $n_{BE}(R_c) = 10^3 \text{ cm}^{-3}$ is assumed. Each cloud rotates rigidly (Ω_0) around the z -axis. The initial temperatures, which are derived from the one-zone model, are different in clouds with different metallicities (see Fig. 1). For example, a cloud with $Z = 0$ (primordial composition) has an initial temperature of 230 K, while a cloud with $Z = Z_\odot$ (solar composition)

has 7 K. As critical Bonnor–Ebert spheres are assumed as the initial state, the radii of the initial spheres are different among models with different metallicities (or different initial temperatures): the radius for models with $Z = 0$ is $5.5 \times 10^5 \text{ AU}$, while that for models with $Z = Z_\odot$ is $1.2 \times 10^5 \text{ AU}$. We confirmed that initial differences in radius do not greatly affect subsequent cloud evolution, in which different cloud sizes but the same metallicity are adopted as the initial state.

To induce fragmentation, the non-axisymmetric density perturbation of the $m = 2$ mode (i.e. the bar mode) $\delta\rho$ is added to the initial cloud:

$$\delta\rho = \begin{cases} A_\phi (r_c/r_p)^2 \cos 2\phi & \text{for } r_c < r_p, \\ A_\phi \cos 2\phi & \text{for } r_c > r_p, \end{cases} \quad (1)$$

where A_ϕ and r_p are the amplitude and effective radius of the density perturbation, respectively, and r_c is the cylindrical radius on the equatorial plane. We adopt A_ϕ as $A_\phi = 10^{-4} - 0.4$, and r_p as $0.1 R_c$ and R_c . Models with $r_p = 0.1 R_c$ have a larger non-axisymmetric perturbation than those with $r_p = R_c$. The initial cloud has a strongly distorted shape in models with large A_ϕ and $R_c = 0.1$. For convenience, we describe the amplitude of the non-axisymmetric perturbation as A_ϕ , in which a capital ‘L’ is added after the value of the amplitude only when $r_p = 0.1 R_c$ is adopted. For example, the model with $A_\phi = 0.1L$ has parameters of $(A_\phi, r_p) = (0.1, 0.1 R_c)$, while that with $A_\phi = 0.1$ has parameters of $(A_\phi, r_p) = (0.1, R_c)$.

The models are characterized by three parameters: the cloud metallicity Z , initial rotation energy β_0 and degree of non-axisymmetric perturbation A_ϕ . The initial rotation energy means the ratio of rotation to gravitational energy in the initial core. The values used for these parameters are $Z = 0 - 1Z_\odot$, $\beta_0 = 10^{-6} - 10^{-1}$, and $A_\phi = 10^{-3} - 0.3$ and $0.1L - 0.4L$. Combining three parameters (Z , β_0 , and A_ϕ), we calculated 480 models.

3 OVERVIEW OF THERMAL EVOLUTION AND ITS CONSEQUENCES FOR PRESTELLAR COLLAPSE

Before discussing fragmentation process, we briefly summarize the outline of thermal evolution with different metallicities (Fig. 1), and see its consequence on dynamical evolution of clouds with very small rotation energy $\beta_0 = 10^{-6}$. For those models, the radial density and velocity profiles are shown in Figures 2 and 3 at some different epochs from the initial state ($\approx 10^4 \text{ cm}^{-3}$) to after the protostar formation ($\geq 10^{21} \text{ cm}^{-3}$).

The thermal evolution of the clouds with $Z = 10^{-6} Z_\odot$ is almost the same as the $Z = 0$ case. For the clouds with $Z = 0$ and $Z = 10^{-6} Z_\odot$, the density and velocity distributions are almost the same. The temperature remains rather high ($\approx 200 \text{ K}$ at $\approx 10^4 \text{ cm}^{-3}$) and increases gradually with the effective ratio of specific heat $\gamma \equiv \partial P / \partial \rho \approx 1.1$. The density gradient in the outer envelope is well approximated by $\propto r^{-2.2}$ (Fig. 2). Even though the cloud becomes optically thick to the H_2 collision-induced absorption at $\approx 10^{16} \text{ cm}^{-3}$, effective cooling by the H_2 dissociation prevents the temperature from rising adiabatically until $\sim 10^{20} \text{ cm}^{-3}$ (Fig. 1), where the dissociation is almost completed. Subsequently,

the growing pressure halts the gravitational collapse at the center and the protostar forms, which is surrounded by accretion shock ($n_c \gtrsim 10^{20} \text{ cm}^{-3}$ at $r \simeq 10^{12} \text{ cm}^{-3}$; Fig. 3) with a radius and mass of $\sim 1 R_\odot$ and $10^{-3} M_\odot$, respectively.

With metal enrichment $Z \geq 10^{-5} Z_\odot$, a striking difference emerges in thermal and dynamical evolution. The clouds become optically thick to the dust in a density around $10^{11} - 10^{15} \text{ cm}^{-3}$, which depends on metallicity in a way that those with lower Z become adiabatic at a higher density, and experience a transient adiabatic phase up to the onset of H_2 dissociation at $\sim 2000\text{K}$ (*first adiabatic phase*, hereafter). Thus, during the first adiabatic phase, a transient hydrostatic core, called the *first core*, appears (indicated by the dotted arrow in Fig. 2). The first core has a size of $\sim 1 \text{ AU}$, and mass of $\sim 0.01 M_\odot$ at its formation. The central temperature of the first core increases with the mass of the first core, which grows by accretion. At $\sim 2000\text{K}$ ($\sim 10^{16} \text{ cm}^{-3}$), the H_2 begins to dissociate and another episode of dynamical collapse begins. This is called the *second collapse phase*, in contrast with the *first collapse phase* before the first adiabatic phase. The evolution thereafter coincides with the zero-metallicity case. Following the end of dissociation ($\simeq 10^{20} \text{ cm}^{-3}$), the temperature increases adiabatically again (the *second adiabatic phase*) and a second hydrostatic-core (the protostar) forms with a similar size as that in zero-metallicity case. Note that two hydrostatic cores (the first core and the protostar) appear in a nested manner, i.e., the protostar forms inside the first core. Correspondingly, two shocks are seen for $Z \geq 10^{-5} Z_\odot$ in Figures 2 and 3. This existence of two adiabatic phases, one at $n_c \sim 10^{11} \text{ cm}^{-3}$ and the other 10^{20} cm^{-3} , during the collapse has an important consequence in fragmentation nature of metal-enriched clouds.

In the model with $Z = 10^{-4} Z_\odot$, three shocks (i.e., three velocity peaks) appear with an extra weak shock at $n_c \simeq 10^9 \text{ cm}^{-3}$ by the rapid H_2 -formation heating at $n_c \simeq 10^8 \text{ cm}^{-3}$ (see, Fig. 1). However, because of the very short duration, no clear adiabatic core is observed at this epoch.

4 DEPENDENCE ON INITIAL CLOUD PARAMETERS

In this section, we see the evolution of clouds with different values of rotation energy β_0 and non-axisymmetric perturbation A_ϕ (i.e., cloud shape) at the initial states. For a given metallicity, the number of combination (β_0, A_ϕ) we calculated amounts to 80. With eight different metallicities $Z = 0 - Z_\odot$, 480 models are calculated in total. The density distributions on the equatorial plane at the end of calculation are presented for different combinations of (β_0, A_ϕ) , which are indicated by the ordinate and abscissa, in Figures 4 - 11 for a given metallicity. The density perturbation is imposed at the scale of the critical radius of the BE sphere R_c for models shown in the first-seventh columns, while at $0.1R_c$ for those in the eighth-tenth columns (indicated by “L”; see, §2). The latter corresponds to models of larger non-axisymmetric perturbation (i.e. more distorted).

4.1 Classification of the Fate of Clouds

The white-and-black-dotted lines in Figures 4 - 11 mark the border between models in which the clouds fragment or not. Each class of models can be classified into two sub-classes, which are indicated by the background colours: the fragmentation models include “fragmentation” (*red*) and “merger” (*violet*) models, while non-fragmentation ones include “non-fragmentation” (*blue*) and “stable-core” (*grey*) models.

Fragments survive without merger in “fragmentation” models, while they merge to form a single core before the end of calculation in “merger” models. The protostars form without fragmentation in the “non-fragmentation” models, while, in the “stable-core” models, the first core remains stable for $\gg 10 t_{\text{ff}}$, where t_{ff} is the local free-fall timescale at the centre. Due to our CPU-time limitation, we failed to follow further cloud evolution for most “stable-core” models. We expect that the first core collapses eventually to form a protostar after angular momentum transfer in a long-term calculation. In fact, for some “stable-core” models, however, we succeeded in following the second collapse and protostar formation and confirmed no fragmentation. Thus, in this paper, we regard the “stable-core” models among the cases of non-fragmentation when we discuss the fragmentation condition.

4.2 Fragmentation Frequency for Different Metallicities

Investigation of Figures 4 - 11 indicates:

(i) the first parameter to determine whether the a rotating spherical cloud fragments or not is the initial rotation parameter β_0 . Although the behavior of the boundary between the two cases is very complicated, the threshold value of β_0 for fragmentation increases with metallicity, being $\beta_0 = 10^{-5}$ for $Z = 0$ while $\beta_0 = 10^{-3}$ for $Z = Z_\odot$. As a result, fragmentation is observed in more models for lower metallicity; 23/60 models for $Z = Z_\odot$, while 47/60 models for $Z = 0$.

(ii) clouds with large non-axisymmetric perturbations develop spiral patterns, which transfer angular momenta by gravitational torque and effectively reduce the rotation parameters β_0 . For example, upward shift of the fragmentation boundary towards larger A_ϕ is seen in the $Z = 10^{-3} - 1Z_\odot$ cases. Similarly, the spirals remove angular momenta from the rotation-supported first cores, which appears for 0.1, and $1Z_\odot$ (Figs. 4 and 5), enabling further collapse to the protostar in large A_ϕ cases. Since the non-axisymmetric perturbation can grow until the higher density phase for a cloud with lower metallicity, fragmentation tends to occur through the bar configuration.

4.3 Spin-up and Fragmentation of Clouds during the Collapse

As seen in Figures 4 - 11, the fragmentation condition depends strongly on the initial rotation rate (β_0) but only weakly on the initial cloud shape (A_ϕ). So far, we used the rotation energy of the whole cloud for easier comparison with observations. It is, however, known that a more important index for cloud evolution and fragmentation is the angular

velocity normalized by the freefall timescale (hereafter the normalized angular velocity),

$$\omega_c \equiv \frac{\Omega_c}{\sqrt{4\pi G \rho_c}}, \quad (2)$$

where Ω_c and ρ_c are the angular velocity and density at the centre of the cloud (Matsumoto & Hanawa 2003, Machida et al. 2004, Machida et al. 2005b). For a uniform sphere with rigid rotation, the normalized angular velocity is related to the rotation energy as

$$\beta_c = \frac{\Omega_c^2 R^3}{3GM} = \frac{\Omega_c^2}{4\pi G \rho_c} = \omega_c^2, \quad (3)$$

where R and M are the radius and mass of the sphere, respectively. Along with the collapse, the clouds spin up and ω_c increases without significant angular momentum transfer. In the case of the primordial ($Z = 0$) clouds, Machida et al. (2008b) found that if the normalized angular momentum reaches the critical value 0.2 - 0.3 (the gray zone in Fig. 12) and thus a thin disk forms owing to centrifugal force before the protostar formation, the disk subsequently fragments into binary or multiples. On the other hand, if the cloud becomes adiabatic and protostar forms before this condition is met, the cloud recovers a spherical shape and does not fragment thereafter.

Here we show that, for higher metallicity, appearance of the first core at lower density put more stringent condition on ω_c for fragmentation. Figure 12 shows evolution of the normalized angular velocity ω_c against the central number density for all cases. Initially, while the centrifugal force is not important, the clouds collapse almost spherically and ω (also, β_c) increases in proportion to $\propto n_c^{1/6}$ ($\beta_c \propto n_c^{1/3}$, respectively). In clouds with rapid initial rotation, ω reaches the critical value $\omega_{\text{frag}} = 0.2 - 0.3$ and the clouds fragment after some more contraction. For $Z \leq 10^{-6} Z_\odot$, the critical value must be attained somewhat before the protostar formation ($\sim 10^{17} \text{ cm}^{-3}$) for $Z \leq 10^{-6} Z_\odot$, as found by Machida et al. (2008b), while for $Z \geq 10^{-5} Z_\odot$ this must be before the first core formation (indicated by the vertical lines in Fig. 12). Since the first cores form at lower density than the protostars, the clouds have a shorter density range to amplify ω in the cases of $Z \geq 10^{-5} Z_\odot$ than the primordial case. In addition, first core appears earlier for higher metallicity. Therefore, an initial higher rotation is required to cause fragmentation for clouds with higher metallicity.

Using the relation $\omega_c \propto n_c^{1/6}$ for spherical collapse, the condition for the normalized angular momentum is amplified from the initial value ω_0 at density n_{ini} to the critical value ω_{frag} before the density n_{adi} where the gas becomes adiabatic is

$$\omega_0 > \omega_{\text{frag}} \left(\frac{n_{\text{adi}}}{n_{\text{ini}}} \right)^{-1/6}. \quad (4)$$

This can be translated to the condition on initial rotation parameter β_0 :

$$\beta_0 > \beta_{\text{frag}} \left(\frac{n_{\text{adi}}}{n_{\text{ini}}} \right)^{-1/3}, \quad (5)$$

where $\beta_{\text{frag}} = \omega_{\text{frag}}^2 = 0.04 - 0.09$.

The adiabatic density n_{adi} and critical rotation parameter $\beta_{0,\text{crit}}$ given by the right-hand side of equation (5) are listed in Table 1 for different values of Z . Here, we used a conservative value of $\beta_{\text{frag}} = 0.1$ is adopted. For

$Z \geq 10^{-5} Z_\odot$, n_{adi} is the density where the clouds become optically thick to dust grains and the first cores form. For $Z \leq 10^{-6} Z_\odot$, where no first adiabatic phase is present, after reaching β_{frag} , the clouds need some more density interval before the protostar for fragmentation and thus $n_{\text{adi}} = 10^{17} \text{ cm}^{-3}$ is adopted as the critical density (see Machida et al. 2008a). These values for $\beta_{0,\text{crit}}$ are in concordance with the results presented in Figures 4 - 11.

4.4 Fragmentation Epochs and Separations

Figure 13 shows the separations at the fragmentation epoch for all fragmentation models. In each panel, the solid line indicates the Jeans length, while the dashed vertical line indicates the beginning of the first adiabatic phase. Note that the separations are about 10 - 100 times the Jeans length since the radial size of the cloud is 10 - 100 times the Jeans scale at fragmentation owing to rotation. With the vertical scale comparable to the Jeans length, the height-to-radius ratio is about 1/10 at this epoch.

For $Z = Z_\odot$, fragmentation events cluster near the upper left corner $n_c = 10^{11} - 10^{14} \text{ cm}^{-3}$, i.e., just after first core formation. For lower metallicity, this distribution extends toward the lower right because the first core forms later and thus fragmentation occurs at a higher density with narrower separation for lower metallicity. For $Z = 10^{-1} Z_\odot$ as well as $10^{-2} Z_\odot$, one fragmentation event is observed at very high density $n_c \sim 10^{20} \text{ cm}^{-3}$ while the rest locate in $10^{10} \text{ cm}^{-3} < n_c < 10^{14} \text{ cm}^{-3}$, which are due to the first-core formation. In some models of $10^{-4} Z_\odot$, fragmentation is observed also before the first-core formation. The abrupt temperature rise at $n_c \simeq 10^8 \text{ cm}^{-3}$ in the $10^{-4} Z_\odot$ clouds (Figs. 2 and 3) temporarily slows the collapse, enabling fragmentation at such an early phase. Without the first-core formation, no clear fragmentation epoch exists for $Z \leq 10^{-6} Z_\odot$. Fragmentation takes place whenever a disk-like configuration appears due to rotation and distributes in a wide range of $10^{10} \text{ cm}^{-3} < n_c < 10^{21} \text{ cm}^{-3}$ (Machida et al. 2008a) although some events at $n_c > 10^{20} \text{ cm}^{-3}$ might be caused by the protostar formation, as in the models with $Z \geq 10^{-5} Z_\odot$ at first-core formation.

Figure 14 shows the frequency distribution of further-most separations between fragments at fragmentation. This shows that binaries with higher metallicity have a wider separation. Those with $Z = Z_\odot$ have separations $10 \text{ AU} < r_{\text{sep}} < 1000 \text{ AU}$, while at $Z = 0$, the range is $r_{\text{sep}} < 10 \text{ AU}$. The separations are distributed in a wide range of $0.1 \text{ AU} < r_{\text{sep}} < 1000 \text{ AU}$ for models with $Z = 10^{-2} - 10^{-5} Z_\odot$.

4.5 Non-axisymmetric Perturbation and Fragmentation Mode

In a few cases in Figures 4 - 11, the clouds fail to fragment even if the condition (eq. 4) is fulfilled. With moderate non-axisymmetry, the cloud can avoid fragmentation even if condition (eq. 4) is fulfilled owing to angular momentum is effectively transferred by the spiral arms. Interestingly, with even larger A_ϕ , the clouds tend to fragment through bar configurations instead of ring configurations realized for fragmentation in small A_ϕ cases. Lower metallicity clouds tend to fragment at higher density. This allows non-axisymmetric

perturbations to grow for a longer time. Thus, fragmentation through the bar is more common for lower metallicity. For example, for $Z = 0$, 33 out of total 47 fragmentations are through the bar mode.

5 DISCUSSION

As shown in §4.3, the fragmentation condition is that the initial rotation energy β_0 must be larger than the threshold value, which increases with the metallicity. Thus, with lower metallicities, clouds with smaller rotation energy can fragment. Observations in the solar neighbourhood have shown that molecular clouds (with solar metallicity) have rotation energies in the range of $10^{-4} < \beta_0 < 0.07$ with an average value of $\beta_0 = 0.02$ (Goodman et al. 1993; Caselli 2002). On the other hand, we cannot observe the initial rotation energies of clouds with lower or zero metallicity. Cosmological simulations have shown that host clouds of star formation have rotation energies of $\beta \approx 0.1$ (Bromm et al. 2002; Yoshida et al. 2006), which is slightly larger than those in molecular clouds. Thus, we expect a higher binary frequency in a lower-metallicity environment (or in the early universe), roughly assuming that host clouds have almost the same distribution of angular momentum (or rotation energy) as observations in the solar neighbourhood. If the lower limit of the rotation energy is $\beta_0 \simeq 10^{-4}$, as in the solar neighbourhood, fragmentation always occurs in clouds with $Z \leq 10^{-4} Z_\odot$, because their fragmentation condition is $\beta_0 > 5 \times 10^{-4}$ (see, Table 1). As a result, the binary frequency increases as the metallicity decreases, and most stars are born as binary or multiple systems in low-metallicity environments.

In our calculation, fragments have masses of $0.1 - 10^{-3} M_\odot$ at fragmentation. This mass range corresponds to that of brown dwarfs or low-mass stars. The mass of fragments increases in the subsequent accretion phase. Since the gas supply (or gas accretion) stops at ejection, ejected fragments with mass of $10^{-3} - 0.1 M_\odot$ are expected to evolve to form a brown dwarf or low-mass star. Thus, our result indicates that even in extremely low- or zero-metallicity environments, substellar-mass objects can form. On the other hand, fragments remaining in the host cloud are expected to increase their mass by accretion and grow to massive stars (or massive star binaries). As a result, we expect that a single massive star (or a massive binary system) and multiple low-mass stars can be formed in a single host cloud. When multiple fragments appear like a star cluster, as shown in the upper left panels of Figures 4 - 11, low-metallicity stars are expected to have two peaks at $10^{-3} - 0.1 M_\odot$ and $100 M_\odot$ in mass distribution. Note that if fragments stay in the cloud for a while and are ejected after acquiring some mass, a star with mass $M \geq 0.1 M_\odot$ can form.

Subsolar-mass stars can form even in low- (or zero-) metallicity environments by the ejection of fragments. Recently, metal-poor stars with $Z < 10^{-5} Z_\odot$ are observed (Christlieb et al. 2002; Frebel et al. 2005; Aoki et al. 2006). Forming in the early universe, they should have a mass of $\lesssim 0.9 M_\odot$. Such low-mass metal-poor stars can form by the fragmentation and ejection mechanism, as described above. In addition, our result allows even the existence of zero-metallicity stars with sub-stellar mass. Our calculation

showed that the binary frequency for zero-metallicity stars is as high as for those with $Z = 10^{-5}$ and $10^{-6} Z_\odot$. Thus, we expect observation of zero-metallicity stars in the future. In addition, as in the cases of $(A_\phi, \beta) = (0.001, 0.1)$ in Figure 6, the binary system can be ejected from the host cloud when multiple fragments appear. Suda et al. (2004) claimed that stars with $Z < 10^{-4} Z_\odot$ are in binaries, because their surface abundance ratios are well explained by mass transfer from an (unobserved) AGB companion. The ejection mechanism may explain the origin of such low- or even zero-metallicity binaries.

In this study, we followed the evolution of fragments and protostars only in their early phase. To determine the final mass and fate of fragments, calculations in the subsequent accretion phase are required.

6 SUMMARY

In this research, we studied the binary/multiple formation process during the collapse of rotating clouds with various metallicities. We found the following results:

(i) A transient hydrostatic core (“first core”) appears during the prestellar collapse for metallicity $\geq 10^{-5} Z_\odot$ at higher density and with smaller size toward lower metallicity. For $Z \leq 10^{-6} Z_\odot$, a protostar directly forms without any transient core.

(ii) When rotation reaches a fraction of Keplerian value before formation of the adiabatic core (i.e., the first core for $\geq 10^{-5} Z_\odot$ or the protostar for $\leq 10^{-6} Z_\odot$), the cloud develops disk-like structure and subsequently fragments into binary/multiples. This condition can be translated to the initial rotation parameter β_0 exceeding a threshold value $\beta_{0,\text{crit}}$. Since lower-metallicity clouds have longer density interval to spin up, i.e. higher density for the adiabatic-core formation, they have smaller threshold value. For example, $\beta_{0,\text{crit}} \sim 10^{-3}$ (10^{-5}) for $Z = Z_\odot$ ($Z = 0$, respectively).

(iii) With modest non-axisymmetric density perturbation, angular momentum transfer by gravitational torque can prevent fragmentation. However, even larger non-axisymmetry causes fragmentation through the bar-mode instability.

(iv) For $Z \geq 10^{-5} Z_\odot$, majority of fragmentation occur just after the first-core formation, while for $Z \leq 10^{-6} Z_\odot$ fragmentation epochs distributes in a wide range of $10^{14} \text{ cm}^{-3} < n_c < 10^{22} \text{ cm}^{-3}$. Clouds with lower metallicity fragments at a higher density with shorter orbital period and their binary separations are narrower. Fragmentation proceeds mainly via the bar configuration in low ($\lesssim 10^{-3} Z_\odot$) metallicity clouds, while via the ring configuration for higher metallicity. The difference in fragmentation modes may affect the subsequent evolution in the accretion phase.

(v) With smaller threshold value for the rotation parameter, more binaries are expected to form from lower metallicity gas. With typical rotation rate for nearby star-forming clouds, most stars with $Z < 10^{-4} Z_\odot$ are born as members of binary/multiple stellar systems. Fragments have the masses of $10^{-3} - 0.1 M_\odot$ at their formation. If they are ejected from the host cloud by three-body interaction before gaining a large amount of mass, substellar-mass objects with extremely low- or even zero-metallicity can form. The observed

stars with $[\text{Fe}/\text{H}] < -5$ might have formed by this mechanism. Moreover, we expect the possible discovery of zero-metallicity stars in the Milky-Way halo. On the other hand, if not ejected, the fragments accrete the ambient gas. In low-metallicity clouds, because the accretion does not stop until the central stars grow to $\gtrsim 100M_{\odot}$ (Omukai & Palla 2001, 2003; McKee & Tan 2008), massive stars or massive binary systems form.

ACKNOWLEDGMENTS

Numerical computations were carried out on VPP5000 at National Astronomical Observatory of Japan. This work was supported by the Grant-in-Aid for the Global COE Program "The Next Generation of Physics, Spun from Universality and Emergence" from the Ministry of Education, Culture, Sports, Science and Technology (MEXT) of Japan, and supported in part by the Grants-in-Aid from MEXT (18740104, 18740113, 18740117, 19047004 KO, 21740136).

REFERENCES

- Abel, T., Bryan, G. L., & Norman, M. L. 2002, *Science*, 295, 93
- Abt, H. A. 1983, *ARA&A*, 21, 343
- Aoki, W., et al., 2006, *ApJ*, 639, 897
- Bodenheimer P., Burkert A., Klein R. I., & Boss A. P., 2000, in Mannings V., Boss A. P., Russell S. S., eds, *Protostars and Planets IV*. Univ. Arizona Press, , p. 675
- Bonnor, W. B. 1956, *MNRAS*, 116, 351
- Bromm, V., Coppi, P. S., & Larson, R. B., 2002, *ApJ*, 564, 23
- Bromm, V., & Loeb, A. 2006, *ApJ*, 642, 382
- Caselli, P., Benson, P. J., Myers, P. C., & Tafalla, M. 2002, *ApJ*, 572, 238
- Christlieb, N., et al. 2002, *Nature*, 419, 904
- Clark, P. C., Glover, S. C. O., & Klessen, R. S. 2008, *ApJ*, 672, 757
- Duquennoy, A., & Mayor, M. 1991, *A&A*, 248, 485
- Ebert, R. 1955, *Z. Astrophys.*, 37, 222
- Fischer, D. A., & Marcy, G. W. 1992, *ApJ*, 396, 178
- Frebel, A., et al. 2005, *Nature*, 434, 871
- Goodwin S. P., Kroupa P., Goodman A., & Burkert A., 2007, in Reipurth B., Jewitt D., Keil K., eds, *Protostars and Planets V*. Univ. Arizona Press, , p. 133
- Goodman, A. A., Benson, P. J., Fuller, G. A., & Myers, P. C. 1993, *ApJ*, 406, 528
- Komiya, Y., Suda, T., Minaguchi, H., Shigeyama, T., Aoki, W., & Fujimoto, M. Y. 2007, *ApJ*, 658, 367
- Machida, M. N., Tomisaka, K., & Matsumoto, T. 2004, *MNRAS*, 348, L1
- Machida, M. N., Matsumoto, T., Tomisaka, K., & Hanawa, T. 2005a, *MNRAS*, 362, 369
- Machida, M. N., Matsumoto, T., Hanawa, T., & Tomisaka, K. 2005b, *MNRAS*, 362, 382
- Machida, M. N., Matsumoto, T., Hanawa, T., & Tomisaka, K. 2006a, *ApJ*, 645, 1227
- Machida, M. N., Omukai, K., Matsumoto, T., & Inutsuka, S.-i. 2008a, *ApJ*, 677, 813
- Machida, M. N. 2008b, *ApJL*, 682, L1
- Mathieu, R. D. 1994, *ARA&A*, 32, 465
- Makino, J. 1996, *ApJ*, 471, 796
- Matsumoto T., & Hanawa T., 2003, *ApJ*, 595, 913
- McKee, C. F., & Tan, J. C. 2008, *ApJ*, 681, 771
- Nomoto, K., Thielemann, F.-K., & Yokoi, K. 1984, *ApJ*, 286, 644
- Omukai, K., Tsuribe, T., Schneider, R., & Ferrara, A. 2005, *ApJ*, 626, 627
- Omukai, K., & Palla, F. 2001, *ApJL*, 561, L55
- Omukai, K., & Palla, F. 2003, *ApJ*, 589, 677
- Saigo, K., Matsumoto, T., & Umemura, M. 2004, *ApJ*, 615, L65
- Seto, N. 2002, *MNRAS*, 333, 469
- Suda, T., Aikawa, M., Machida, M. N., Fujimoto, M. Y., & Iben, I. J. 2004, *ApJ*, 611, 476
- Sugimoto, D. & Bettwieser, E. 1983, *MNRAS*, 204, 19P
- Yoshida N., Omukai K., Hernquist L., & Abel T., 2006, *ApJ*, 652, 6
- Yoshida, N., Omukai, K., & Hernquist, L. 2008, *Science*, 321, 669

Table 1. Fragmentation conditions for each metallicity

Metallicity	$(n_{\text{adi}}/10^4 \text{ cm}^{-3})$	$\beta_{0,\text{crit}} (n_{\text{ini}}/10^4 \text{ cm}^{-3})^{1/3}$
Z_{\odot}	3×10^7	3.2×10^{-4}
$10^{-1} Z_{\odot}$	10^8	2.2×10^{-4}
$10^{-2} Z_{\odot}$	7×10^8	1.1×10^{-4}
$10^{-3} Z_{\odot}$	10^9	10^{-4}
$10^{-4} Z_{\odot}$	10^{10}	4.6×10^{-5}
$10^{-5} Z_{\odot}$	10^{11}	2.1×10^{-5}
$\leq 10^{-6} Z_{\odot}$	10^{13}	4.6×10^{-6}

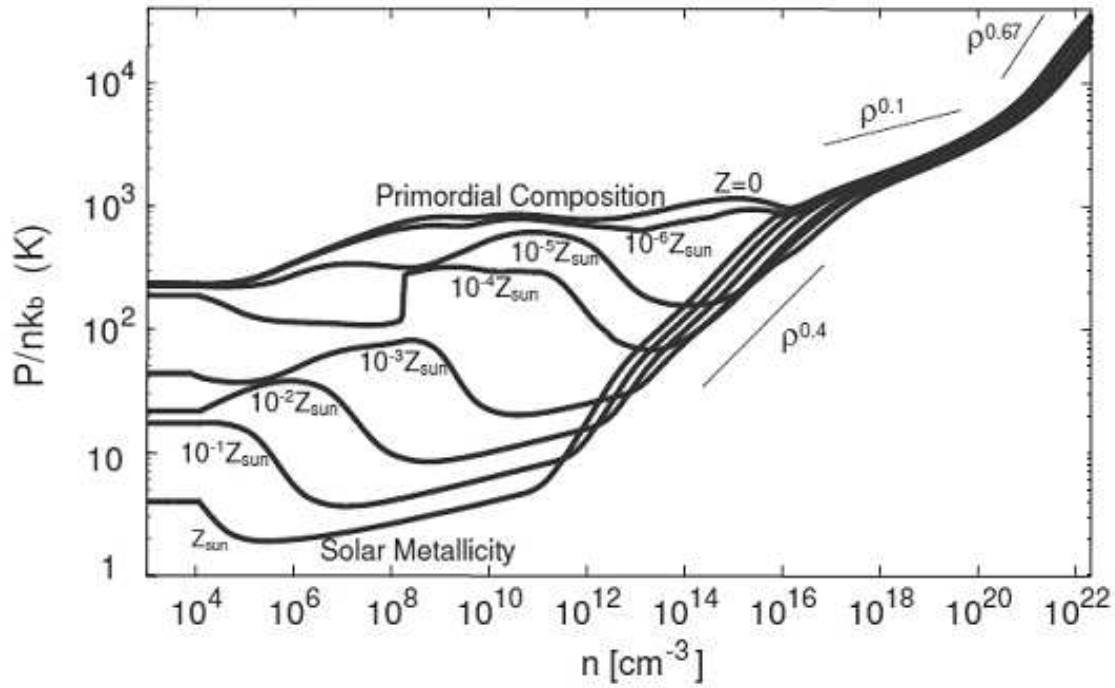


Figure 1. Thermal evolution of collapsing clouds with different metallicities ($Z = 0, 10^{-6}, 10^{-5}, 10^{-4}, 10^{-3}, 10^{-2}, 10^{-1}$ and Z_{\odot}) against the number density. To stress the variation of pressure with density, $P/nk_b = T/\mu$ is plotted, where μ is the mean molecular weight.

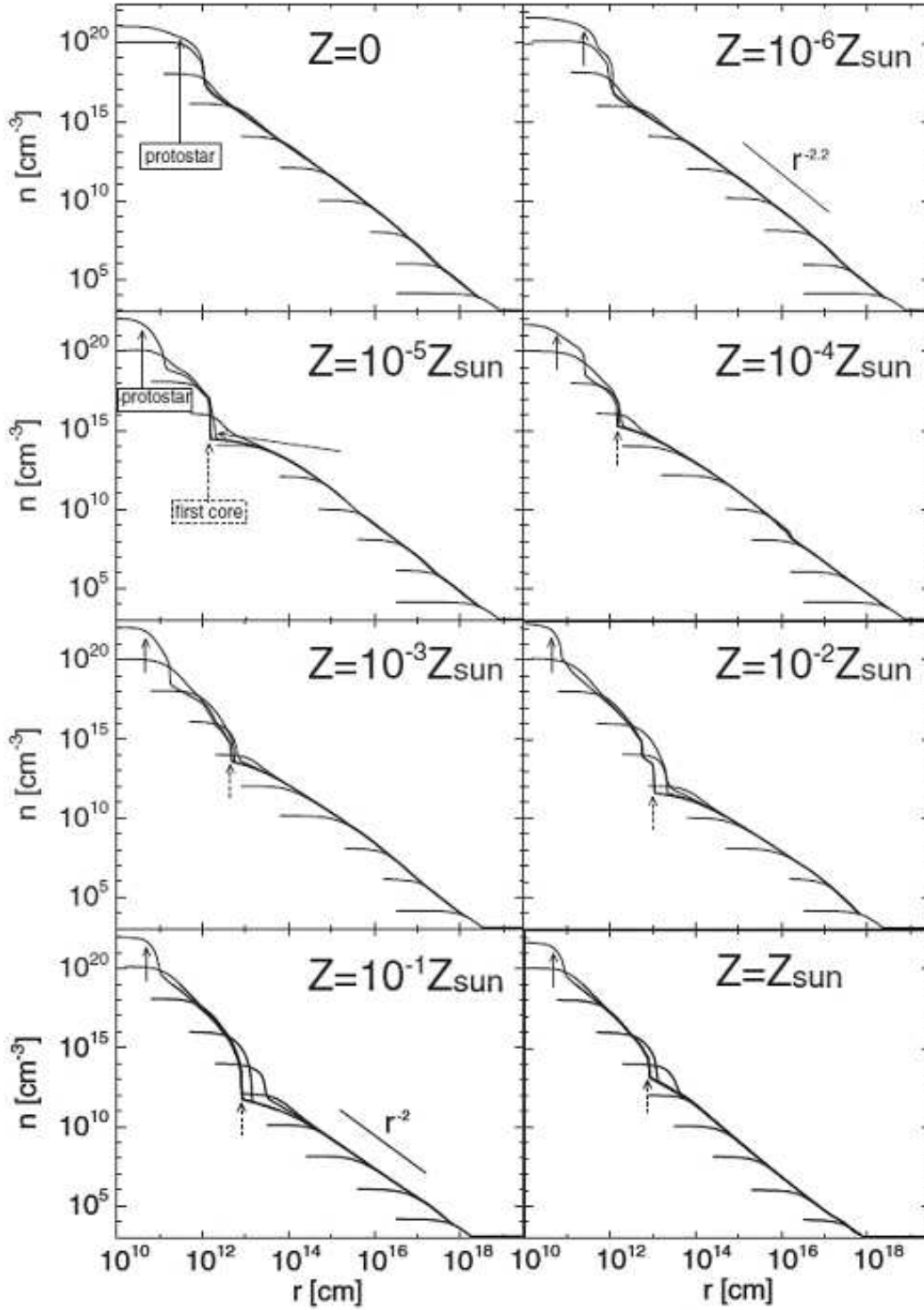


Figure 2. Evolution of radially-averaged density profiles for clouds with different metallicity. Profiles at different times are plotted in the same panel for the same cloud. Formation epochs of the protostar and first core are indicated by solid and dotted arrows, respectively. The relations $r^{-2.2}$ and r^{-2} are also shown in the top right and bottom left panels, respectively.

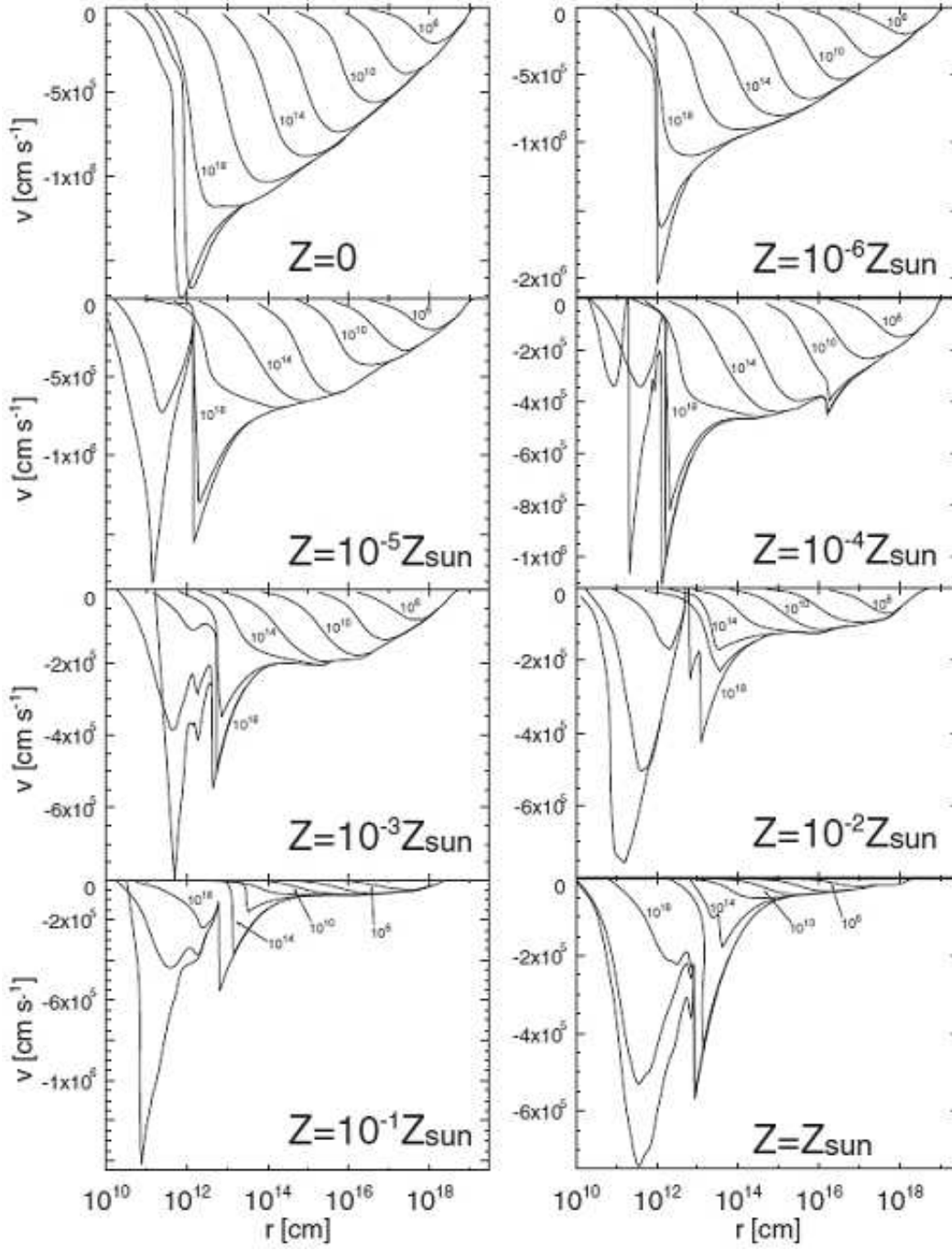


Figure 3. Evolution of radially-averaged velocity profiles for clouds with different metallicity. Numbers in each panel indicate the velocity profiles at epochs $n_c = 10^6, 10^{10}, 10^{14}$ and 10^{18} cm^{-3} .

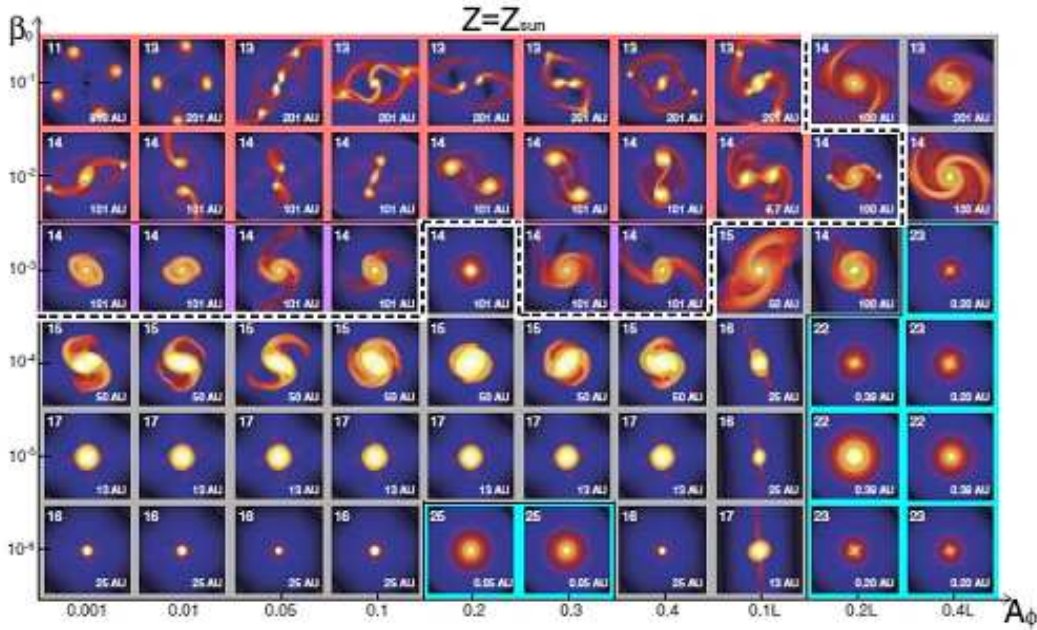


Figure 4. Final outcomes of cloud collapse for metallicity $Z = Z_{\odot}$ for different combinations of the initial amplitude of non-axisymmetric perturbation A_{ϕ} and rotation parameter β_0 . The density distribution (colour-scale) around the centre of the cloud on the equatorial plane is plotted in each panel. The grid level l and grid scale are shown at the upper-left and lower-right corners, respectively, of each panel. The colours of the panel frame indicate the classifications: *red*: fragmentation, *violet*: merger, *blue*: non-fragmentation, and *grey*: stable-core models. The white-and-black dotted line indicates the border between fragmentation (fragmentation and merger models) or not (non-fragmentation and stable-core models).

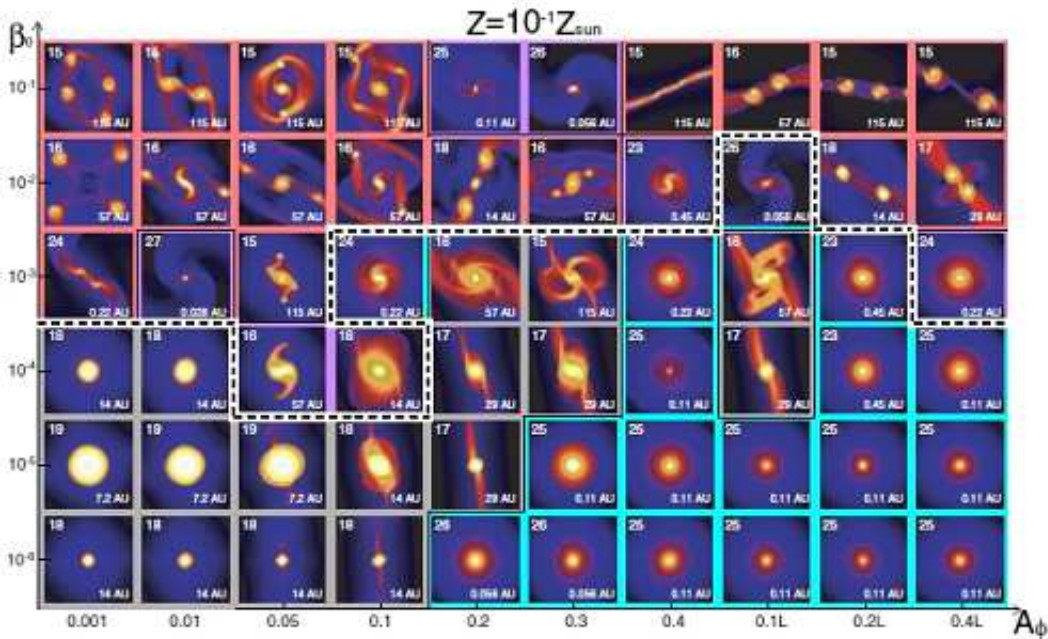


Figure 5. Same as Fig. 4, but for $Z = 10^{-1} Z_{\odot}$ with gray-scale.

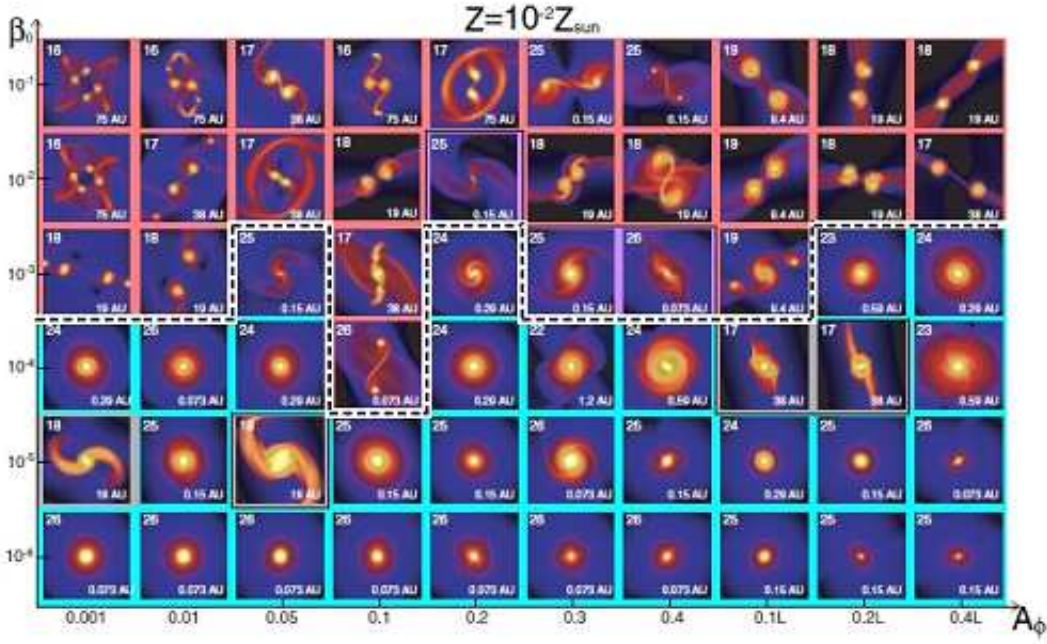


Figure 6. Same as Fig. 4, but for $Z = 10^{-2}Z_{\odot}$.

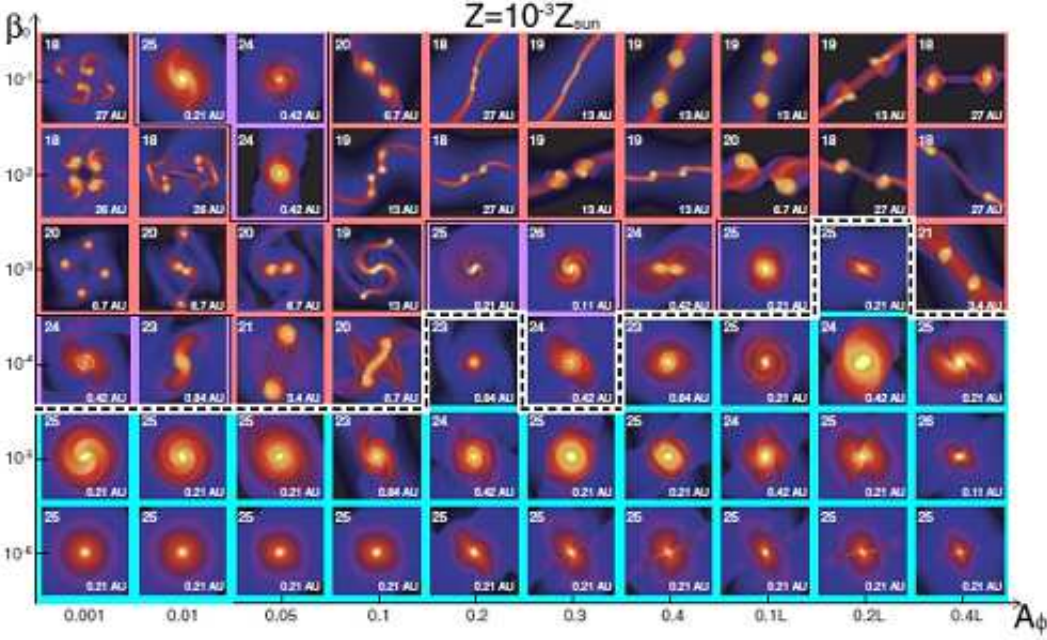


Figure 7. Same as Fig. 5, but for $Z = 10^{-3}Z_{\odot}$.

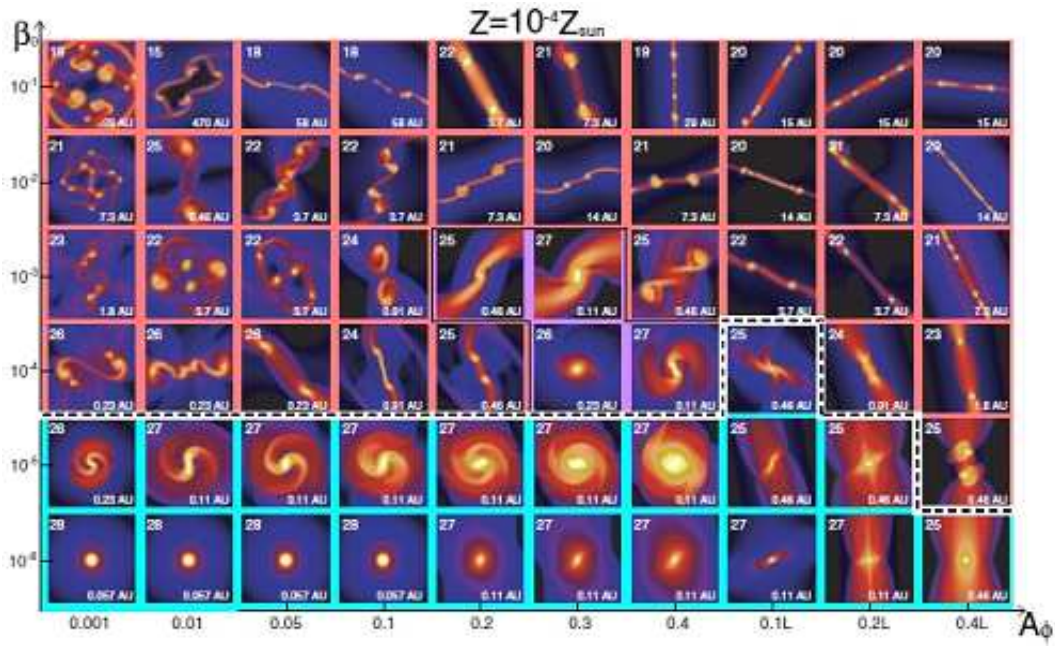


Figure 8. Same as Fig. 4, but for $Z = 10^{-4} Z_\odot$

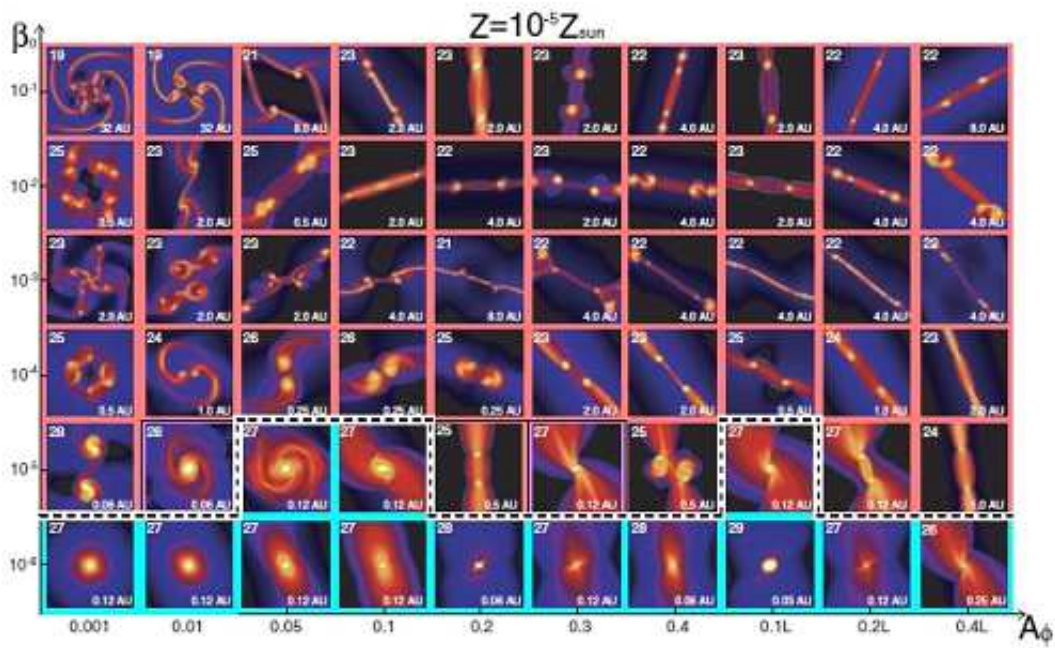


Figure 9. Same as Fig. 5, but for $Z = 10^{-5} Z_\odot$

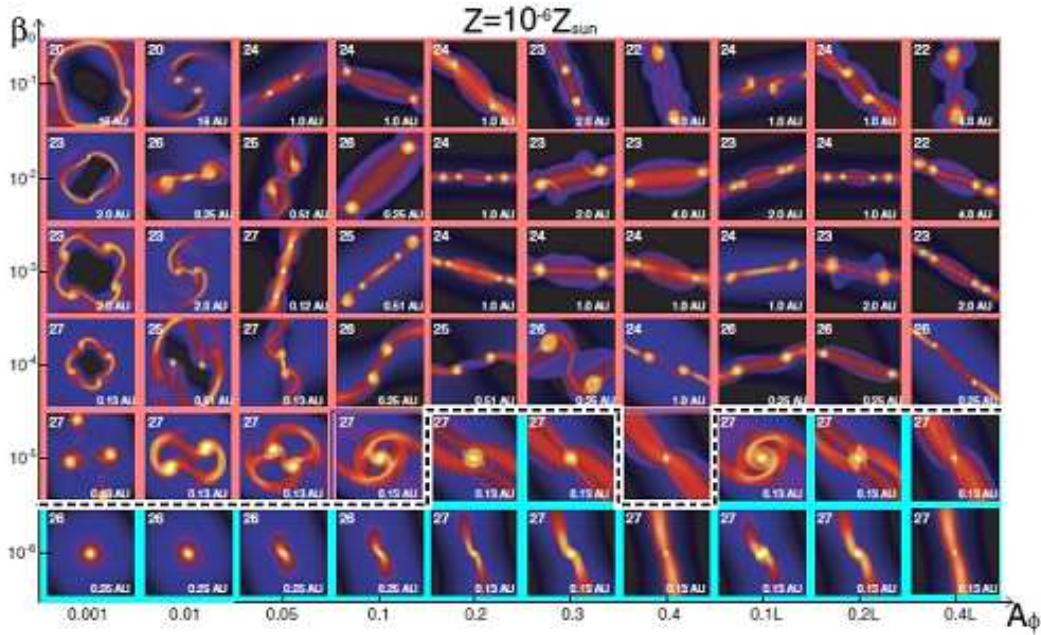


Figure 10. Same as Fig. 4, but for $Z = 10^{-6} Z_{\odot}$

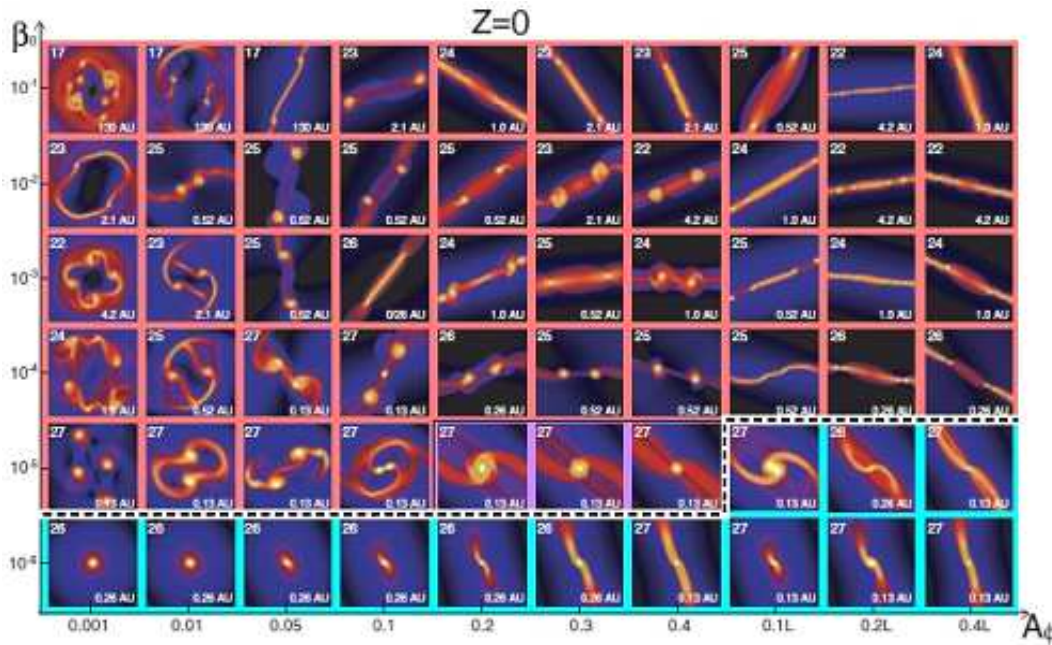


Figure 11. Same as Fig. 5, but for $Z = 0$

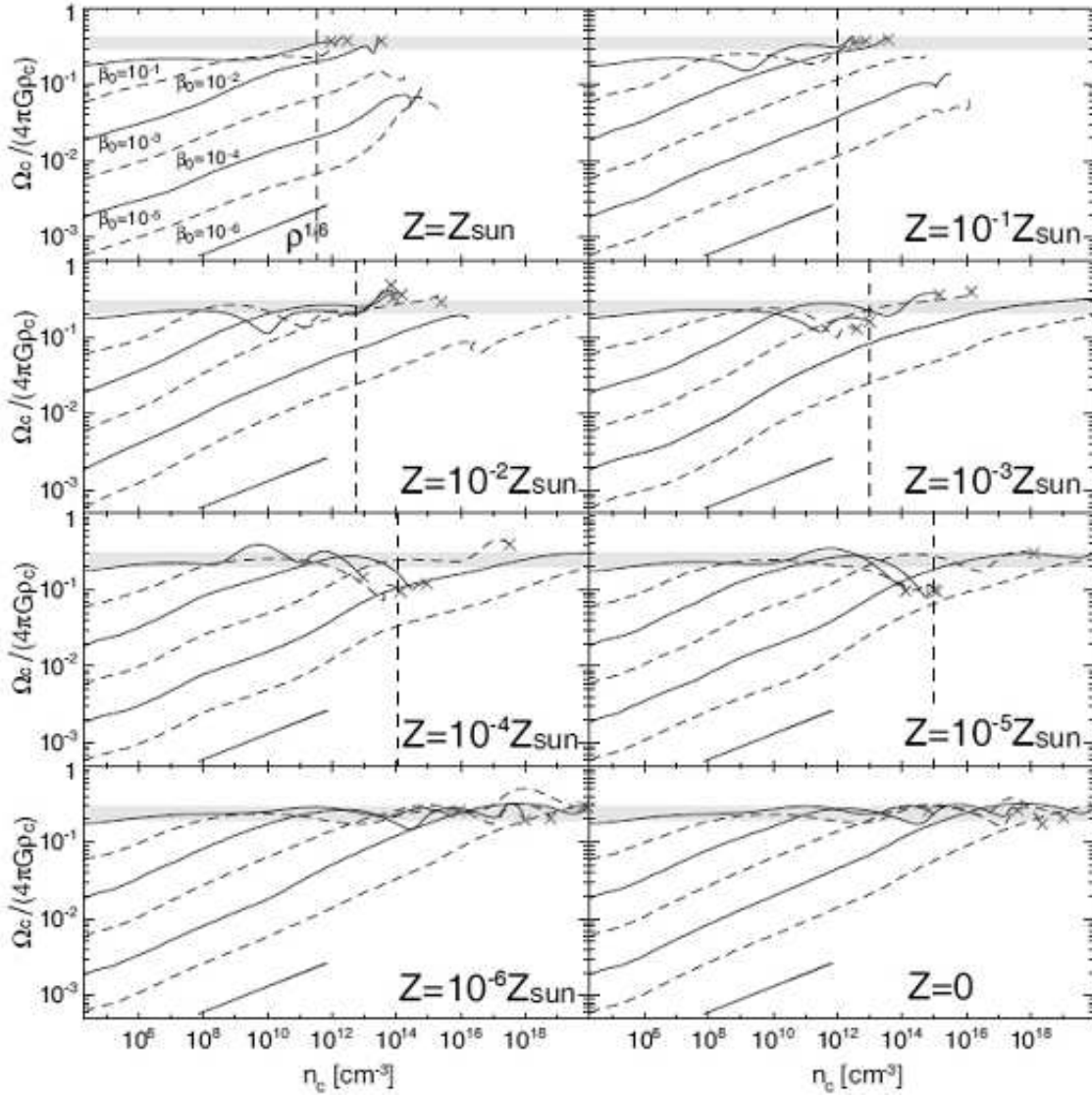


Figure 12. Evolution of the normalized angular velocities at the centre against the number density. Models with the same A_ϕ ($= 0.01$) but different β_0 ($= 10^{-1}$ – 10^{-6}) are plotted in the same panels for the same metallicities. The cases with $\beta_0 = 10^{-1}$, 10^{-3} and 10^{-5} are indicated by solid lines, and those with $\beta_0 = 10^{-2}$, 10^{-4} , and 10^{-6} by dashed lines. The relation $\propto \rho^{1/6}$, valid for spherical collapse, is also shown by a solid line in each panel. The vertical broken line indicates the epoch when the gas first becomes adiabatic.

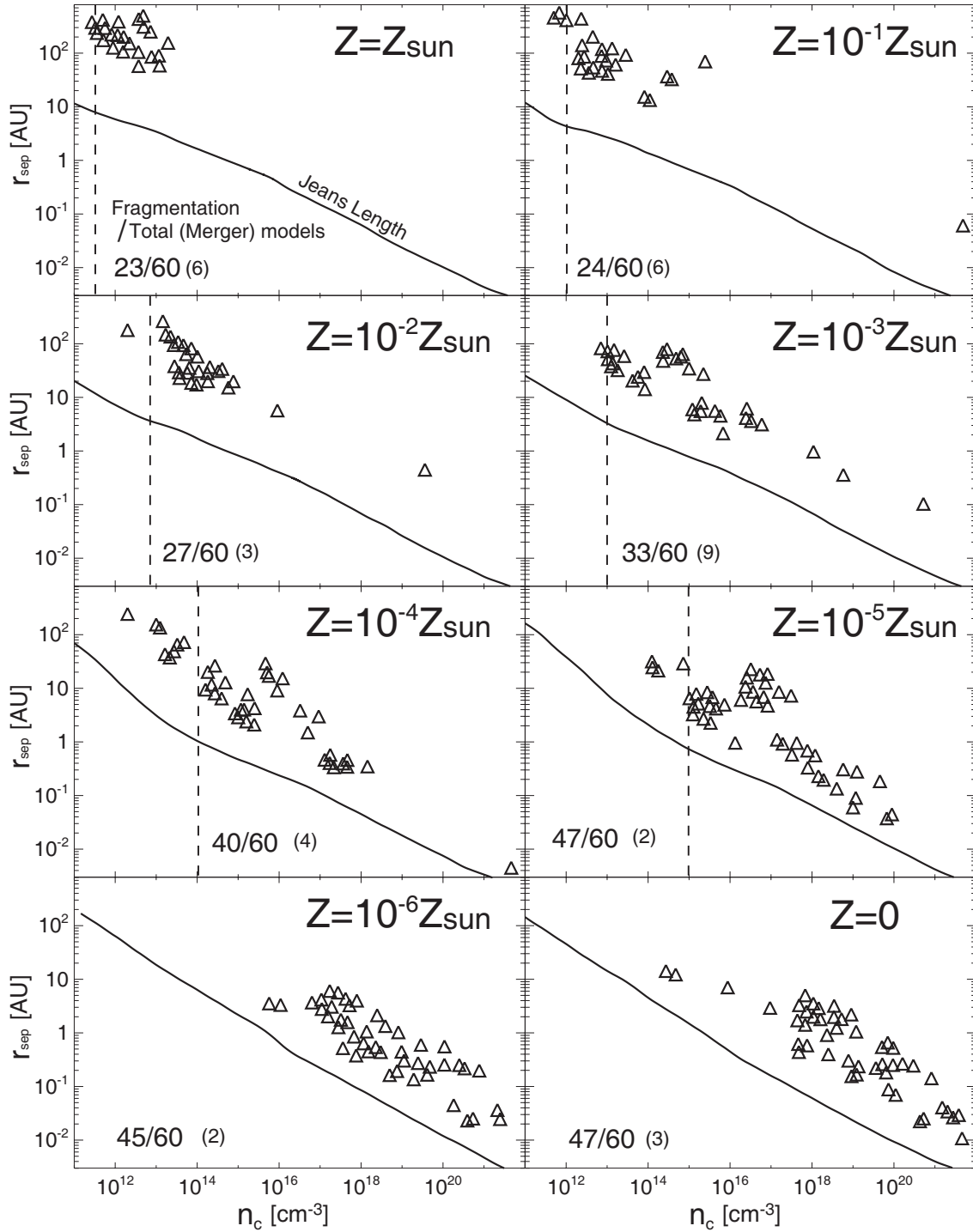


Figure 13. The number density and separation of fragments at the fragmentation epoch. All fragmentation models are plotted for each metallicity. The separation corresponds to the furthestmost distance between fragments. The number of fragmentation models is given at the lower left in each panel, while the number of merger models is indicated by the figure in parentheses. The Jeans length is also illustrated by solid lines. The vertical broken line indicates the epoch when the gas first becomes adiabatic.

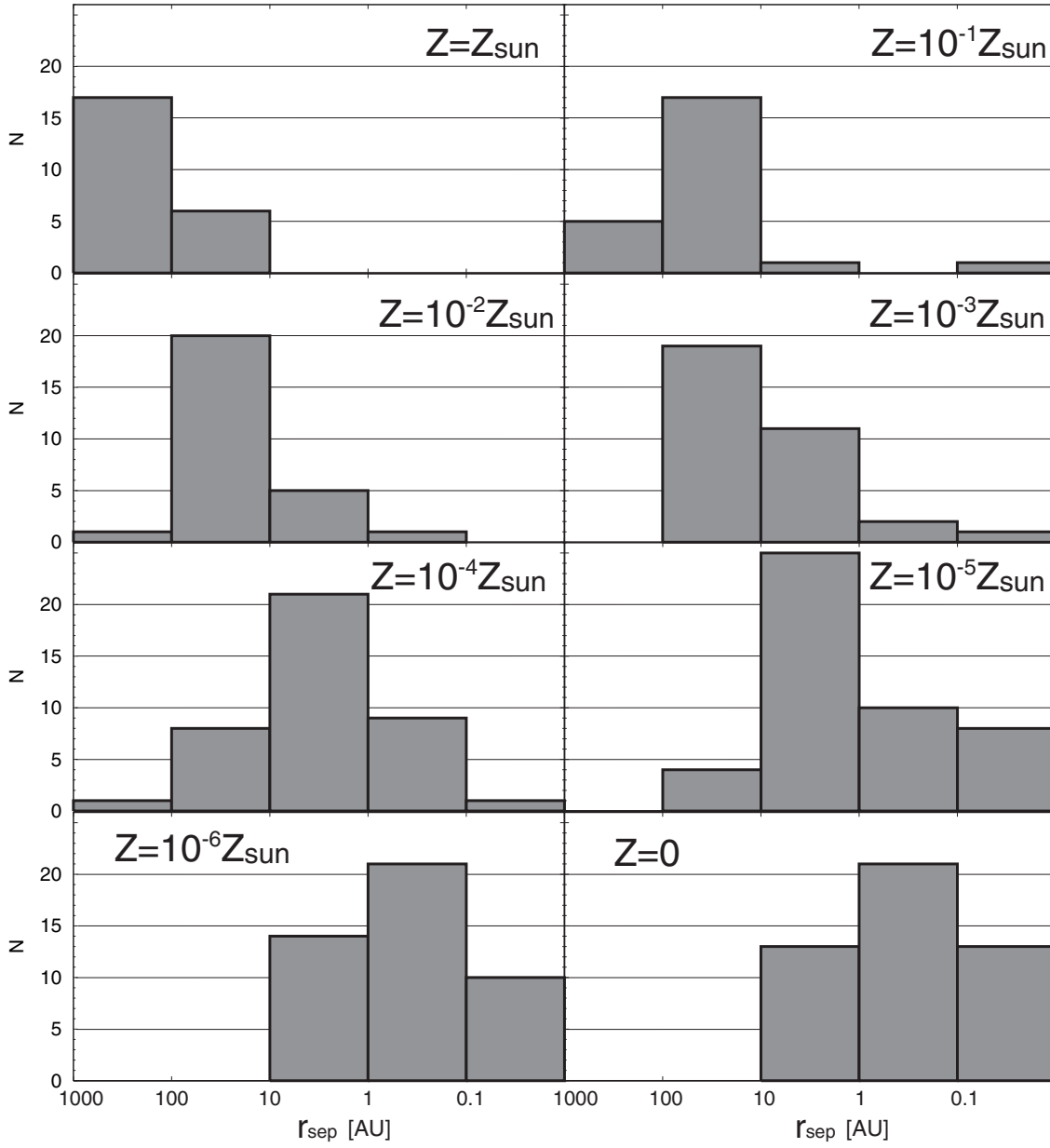


Figure 14. Histogram of the binary separation r_{sep} at fragmentation for all fragmentation models. The metallicity is indicated in each panel.